

UC Riverside

UC Riverside Previously Published Works

Title

Cellular Subcompartments through Cytoplasmic Streaming

Permalink

<https://escholarship.org/uc/item/7r99c4tt>

Journal

Developmental Cell, 34(4)

ISSN

1534-5807

Authors

Pieuchot, Laurent
Lai, Julian
Loh, Rachel Ann
[et al.](#)

Publication Date

2015-08-01

DOI

10.1016/j.devcel.2015.07.017

Copyright Information

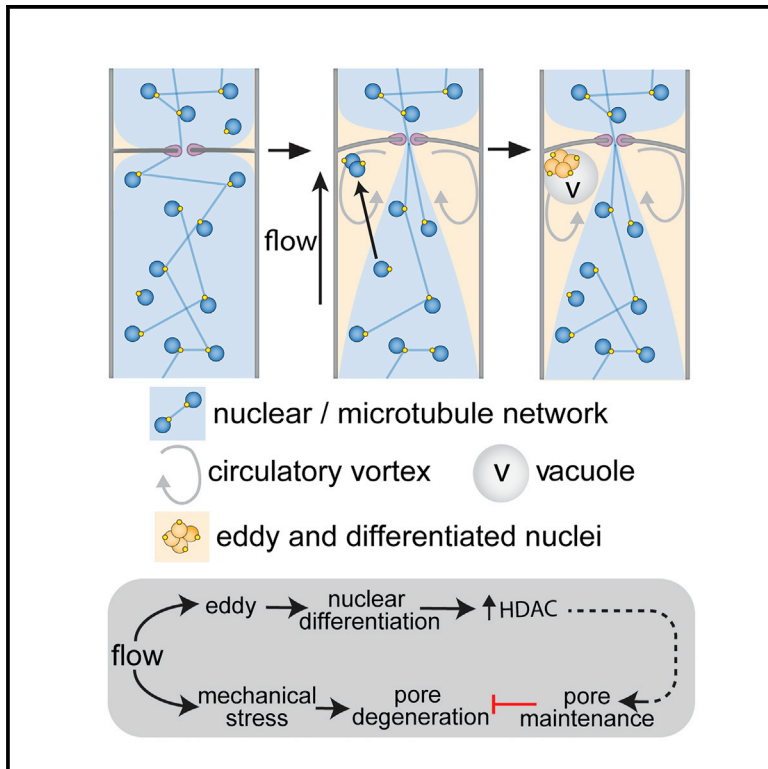
This work is made available under the terms of a Creative Commons Attribution-NonCommercial-NoDerivatives License, available at <https://creativecommons.org/licenses/by-nc-nd/4.0/>

Peer reviewed

Developmental Cell

Cellular Subcompartments through Cytoplasmic Streaming

Graphical Abstract



Authors

Laurent Pieuchot, Julian Lai, Rachel Ann Loh, ..., Keng-Hwee Chiam, Jason Stajich, Gregory Jedd

Correspondence

gregory@tll.org.sg

In Brief

Pieuchot et al. examine intercellular cytoplasmic streaming in the model fungus *Neurospora crassa* and show how biologically distinct subcompartments can be self-organized as a consequence of regimented cytoplasmic streaming.

Highlights

- Cytoplasm streams directionally through fungal septal pores
- Flow engenders microfluidic eddies on the upstream side of the septum
- Nuclei flow in a microtubule network but can be detached and trapped in eddies
- Trapped nuclei accumulate markers required to stabilize flow-stressed pores



Cellular Subcompartments through Cytoplasmic Streaming

Laurent Pieuchot,¹ Julian Lai,¹ Rachel Ann Loh,¹ Fong Yew Leong,² Keng-Hwee Chiam,³ Jason Stajich,⁴ and Gregory Jedd^{1,*}

¹Temasek Life Sciences Laboratory and Department of Biological Sciences, The National University of Singapore, Singapore 117604, Singapore

²Institute of High Performance Computing, A*STAR, Singapore 138632, Singapore

³Bioinformatics Institute, A*STAR, Singapore 138671, Singapore

⁴Department of Plant Pathology & Microbiology and Institute for Integrative Genome Biology, University of California-Riverside, Riverside, CA 92521, USA

*Correspondence: gregory@tll.org.sg

<http://dx.doi.org/10.1016/j.devcel.2015.07.017>

SUMMARY

Cytoplasmic streaming occurs in diverse cell types, where it generally serves a transport function. Here, we examine streaming in multicellular fungal hyphae and identify an additional function wherein regimented streaming forms distinct cytoplasmic subcompartments. In the hypha, cytoplasm flows directionally from cell to cell through septal pores. Using live-cell imaging and computer simulations, we identify a flow pattern that produces vortices (eddies) on the upstream side of the septum. Nuclei can be immobilized in these microfluidic eddies, where they form multinucleate aggregates and accumulate foci of the HDA-2 histone deacetylase-associated factor, SPA-19. Pores experiencing flow degenerate in the absence of SPA-19, suggesting that eddy-trapped nuclei function to reinforce the septum. Together, our data show that eddies comprise a subcellular niche favoring nuclear differentiation and that subcompartments can be self-organized as a consequence of regimented cytoplasmic streaming.

INTRODUCTION

Cellular subcompartments are a defining feature of eukaryotic cells. Membrane-delimited organelles provide a fundamental means of compartmentation wherein specific processes are organized within a controlled microenvironment. Subcompartments can also form in the absence of membranes when multivalent protein-protein and protein-RNA interactions drive the formation of high-order cytoplasm- and nucleoplasm-based assemblies (Brangwynne et al., 2009; Hyman and Brangwynne, 2011; Kato et al., 2012; Lee et al., 2013). Motor proteins that move on cytoskeletal elements play a key role in determining organelle distribution. Motor-driven transport can entrain bulk cytoplasmic streaming, which generally functions to promote advective transport (Goldstein et al., 2008; Woodhouse and Goldstein, 2013), and serves a wide variety of biological functions: In animals, it can trigger symmetry breaking through trans-

port of PAR proteins (Goehring et al., 2011), position the meiotic spindle (Yi et al., 2011), influence morphogen gradients (Hecht et al., 2009), and promote polarized mRNA localization (Palacios and St Johnston, 2002). In plants, streaming promotes long distance transport (Goldstein et al., 2008), as in giant algal cells (Woodhouse and Goldstein, 2013) and pollen tubes (Hepler et al., 2001), and the velocity of streaming has recently been shown to determine plant cell size, presumably through transport of cell growth effectors (Tominaga et al., 2013).

Cytoplasmic streaming also occurs in multicellular fungal hyphae where pores at the center of the septum permit cytoplasm, organelles, and in some cases nuclei, to flow directionally from cell to cell (Abadeh and Lew, 2013; Bleichrodt et al., 2013; Buller, 1933; Ramos-García et al., 2009; Roper et al., 2013). Flow allows individual cells to cooperate (Trinci, 1973) to support rapid invasive tip growth of saprotrophic and pathogenic fungi alike. In *Neurospora*, intercellular streaming also drives the mixing of genetically heterogeneous nuclei, and thereby promotes genetic diversity within the colony (Roper et al., 2013). In contrast to motor-driven streaming in animals and plants, in the fungal hypha, osmotic pressure gradients drive bulk cytoplasmic streaming (Abadeh and Lew, 2013; Lew, 2005, 2011). Beyond this key distinction, little is known about how fungal cytoplasmic streaming is patterned and its impact on cellular organization.

RESULTS

Hyphal Compartments Cooperate to Promote Rapid Tip Growth

The fungal colony undergoes a maturation process as it develops from unicellular spores to a multicellular hyphal network. We initiated this study by making movies to document this process in *Neurospora crassa*. As the hypha increases in length, its rate of tip growth accelerates over a period of around 24 hr to eventually reach a maximum of approximately 1 $\mu\text{m/s}$ (Figure 1 and Movie S1). Branches produced by the primary hypha generally grow more slowly. However, from their inception, their rate of tip growth also increases with increasing length of the primary hypha. Together, these data demonstrate a tissue-like property of the fungal colony wherein hyphal length is correlated to the rate of tip growth.

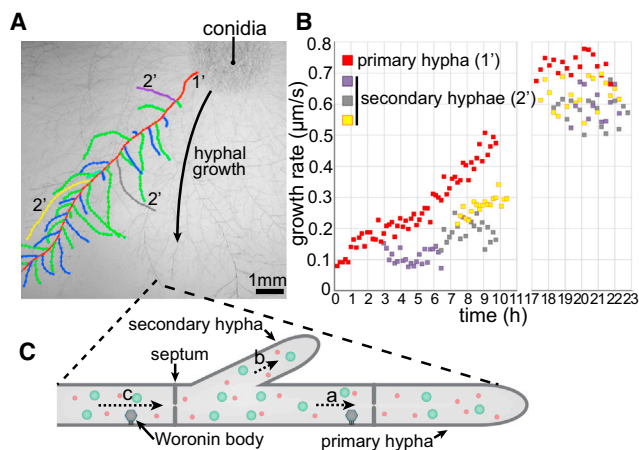


Figure 1. Cellular Cooperativity in the Multicellular Hypha

(A) For a selected hypha, the position of the hyphal tip in primary (red) and secondary (other colors) hyphae is marked every ten minutes. Scale bar represents 1 mm.

(B) The instantaneous growth rate is calculated at each time point. Note that the growth rate of the hypha gradually increases over time, reflecting the contribution of sub-apical compartments to tip growth. Data for time points between 17 and 23 hr was extracted from a second movie of the same colony. (C) The cartoon depicts the structure of a primary and secondary hypha. The septum with its central pore and cortex tethered Woronin bodies are indicated. The length of the dotted arrows (labeled a, b, and c) is proportional to the rate of cytoplasmic flow, which is determined by the rate of upstream tip expansion. Note that the rate of flow at position c is given by the addition of flow rates at positions a and b. Nuclei (green) and organelles (red) are depicted below their actual density. This figure is related to [Movie S1](#).

Cytoplasmic Flow Does Not Conform to Expectations of a Newtonian Fluid

Cell-to-cell cytoplasmic streaming accompanies the development of rapid tip growth. The velocity of streaming is variable and depends on the number of growing tips that are being fed cytoplasm by a given segment of the hyphal network ([Figure 1C](#)). To investigate the nature of high velocity flow, we focused on the septum of primary hyphae approximately 0.5 cm behind apical compartments and quantified the movement of nuclei and peroxisomes by time-lapse confocal microscopy. Both compartments can readily be observed flowing at rates of approximately 20 $\mu\text{m/s}$ ([Figures 2A and 2B](#) and [Movie S2](#)). The maximum rate of tip growth is around 1 $\mu\text{m/s}$, indicating that these hyphal segments are feeding cytoplasm to dozens of downstream hyphal tips.

Fluid mechanics necessitates that streaming velocity increases in proportion to the degree of constriction imposed by the pore. Indeed, both compartments accelerate as they approach the pore to reach peak measured velocities in excess of 200 $\mu\text{m/s}$. On the entry side of the septum, the cytoplasm accelerates along a long, converging path. In contrast, the flow decelerates more rapidly on the exit side of the septum, and along a wider, diverging path ([Figures 2A and B](#)). To determine whether this pattern conforms to expectations of fluid mechanics, we simulated pressure driven flow of an idealized Newtonian fluid through a cylinder of hyphal dimensions ([Figure 2C](#)). Due to the viscous nature of the flow, the acceleration and deceleration profiles are symmetric in the plane of the septum ([Figure 2C](#)). Thus,

flow observed within the hypha does not conform to expectations of Newtonian viscous flow.

Streaming Engenders Conspicuous Upstream Eddies

Flow approaching the septal pore produces regions of relatively stagnant cytoplasm that occur where the septum meets the lateral cell wall. In this area, peroxisome and nuclei can flow in the reverse direction indicating the presence of vortices ([Figure 2A](#) and [Movie S2](#)). We refer to these regions as eddies. Nuclei closely associated with the cell cortex tend to be excluded from the flow, and this effect appears to be more pronounced in the region of eddies ([Figure 2D](#)). Large vacuoles can also become immobilized on the upstream side of the septum and excluded from flow ([Figure 2E](#)). These vacuoles are seen at the second to third septum of primary hyphae, indicating that they form soon after deposition of the septum. Indeed, eddy-trapped vacuoles can increase their diameter by many microns in less than a minute ([Figure 2E](#)), presumably by fusing with smaller vacuoles that arrive with the flow.

Microtubules Contribute to Non-Newtonian Flow

In *Neurospora*, long cytoplasmic microtubules emanate from nuclear spindle pole bodies (SPBs) ([Freitag et al., 2004](#); [Ramos-García et al., 2009](#)). To examine their behavior in flow, we made movies using a strain expressing a β -tubulin-GFP fusion protein ([Freitag et al., 2004](#)). Flowing microtubules have a more or less random orientation upstream of the septum, but become aligned parallel to the long axis of the hypha as they approach the pore ([Figures 3A and 3B](#) and [Movie S3](#)). This orientation is rapidly lost on the downstream side of the septum, and overall, this asymmetric pattern is similar to that observed for flowing peroxisomes and nuclei ([Figure 2](#)).

When flowing microtubules enter the high-velocity flow-field near the pore, they are expected to accelerate along their entire length. This would tend to entrain flow to promote a funnel-shaped entry path. In contrast, deceleration upon pore exit promotes microtubule relaxation and would tend to diminish entrainment resulting in a broader exit path. Computer simulation of an idealized microtubule bundle in a Newtonian viscous flow corroborates this view. As opposed to the symmetric flow observed when simulations are conducted in the absence of microtubules ([Figure 2C](#)), their presence leads to asymmetric flow across the septum and the formation of upstream vortices ([Figure 3C](#)).

To directly assess the role of microtubules, we employed the microtubule depolymerizing drug nocodazole. Because microtubules are required for growth, and flow only occurs in growing hyphae, we employed a drug concentration that inhibits hyphal extension by approximately fifty percent. In the presence of nocodazole, long cytoplasmic microtubules are not observed, rather the microtubule tag produces a mostly punctate signal ([Figure 3D](#)). We quantified the movement of nuclei in hyphae that had similar rates of flow. These data show that when cytoplasmic microtubules are depolymerized, the distance from the septum at which nuclei begin to accelerate is significantly reduced ([Figure 3D](#)). To quantify this effect, we used the statistical measure skewness (see [Experimental Procedures](#)). Where a value of 0 refers to perfectly symmetrical flow, the skewness of the velocity distribution is reduced from 1.83 for control hyphae to 0.45 for nocodazole treated hyphae.

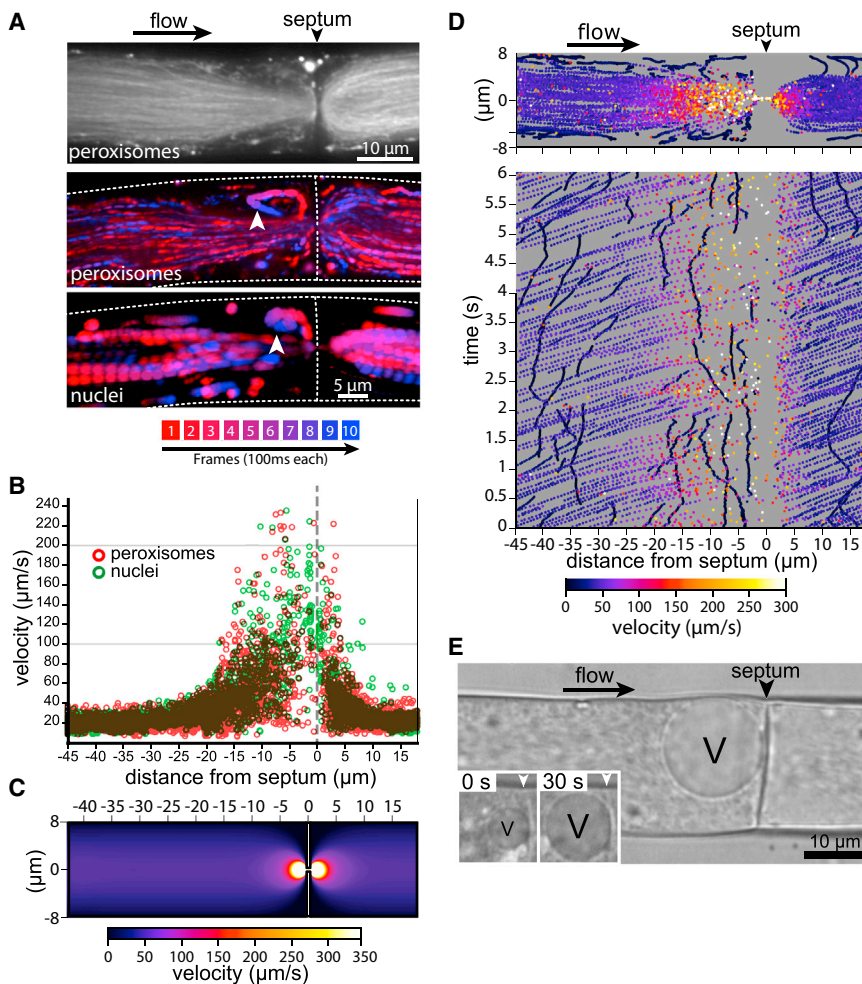


Figure 2. Cytoplasmic Streaming through the Primary Hypha

(A) A maximum projection shows the pattern of flow of peroxisomes as they approach and exit the pore (upper). Scale bar represents 10 μm . The movement of peroxisomes (middle panel) and nuclei (lower) is shown over ten successive frames. Scale bar represents 5 μm . Time is indicated by coloring each frame from magenta to blue according to the scale provided. Arrowheads point to eddy-localized organelles that reverse their direction of movement. Direction of flow is indicated by an arrow. This figure is related to [Movie S2](#).

(B) The instantaneous velocity of peroxisomes and nuclei is shown with respect to the position of the septum. Note that flow is asymmetric in the plane of the septum.

(C) Computer simulation of a Newtonian flow through a model hypha, whose hyphal radius is 8 μm , pore radius is 0.2 μm and septal wall thickness 0.4 μm . The speed of flow is color coded according to the scale shown at the bottom. Note that simulated flow is symmetrical in the plane of the septum. Scale is indicated on the y axis. See [Experimental Procedures](#) for additional information.

(D) Cortex associated nuclei resist flow. The instantaneous velocity of nuclei is coded according to the color scale found at the bottom of the figure. The lower panel plots the data as a kymograph showing time (y axis) against distance from the septum (x axis). Note that slowly moving cortex associated nuclei tend to stop moving on the upstream side of the septum. Scale is indicated on the x axis.

(E) Vacuoles in the eddy. The still image shows a large eddy-trapped vacuole (V). Inset: images showing maturation of an eddy-trapped vacuole at a young primary septum (third septum from the hyphal tip). It shows the near doubling of vacuole (V) diameter within 30 s. Arrowheads point to the septum. Scale bar represents 10 μm .

Thus, microtubules indeed contribute to entrainment of asymmetric flow. Interestingly, flow asymmetry and upstream vortices are not abolished by microtubule depolymerization, suggesting that additional factors contribute to the patterning of non-Newtonian flow.

Streaming Causes Mechanical Stress to the Septum

Septa engaged in vigorous streaming undergo periodic deflections and bend forward in the direction of flow to become concavo-convex ([Figure 3E](#) and [Movie S4](#)). Most of the observed deflections correlate with the occurrence of nuclei passing through the pore ([Figure 3F](#) and [Movie S5](#)). We mathematically modeled the magnitude of the pressure difference caused by transient pore plugging using the measured maximum deflection and values for cell wall elasticity obtained by atomic force microscopy ([Zhao et al., 2005](#)). Using Kirchhoff-Love plate theory, we estimate a deflection-associated pressure difference of approximately 2 bar (see [Experimental Procedures](#)). This correlates well with the documented hyphal hydrostatic pressure of about 4–5 bar ([Lew et al., 2004](#)). These observations indicate that pressure-driven flow imparts significant mechanical force to the septum and pore.

Genetic Maintenance of the Flow-Stressed Septum

We previously used machine learning to identify a group of intrinsically disordered septal pore associated (SPA) proteins that localize to the septal pore ([Lai et al., 2012](#)). One of these, SPA-19, was initially considered a false-positive based on its localization to the nucleus. However, examination of its deletion phenotype suggests an important role in the maintenance of septa engaged in streaming. Young septal pores found at the periphery of the colony have similar dimensions in wild-type and the *spa-19* deletion strain. However, as the mutant hyphae ages, the septum cell wall breaks down and pores become aberrantly enlarged ([Figure 4A](#)). These pores are too large for occlusion by Woronin bodies, which normally seal septal pores when hyphal compartments are damaged ([Jedd and Chua, 2000](#)) and consequently, the mutant bleeds protoplasm in sub-apical but not apical regions of the colony ([Figures 4B](#) and [4C](#)). Septum breakdown is observed in primary hyphae, where streaming is extensive, but not in less active secondary hyphae ([Figure 4A](#)), suggesting that it is triggered by flow. These data suggest that *spa-19* plays a key role in protecting the septum from wear-and-tear associated with vigorous cytoplasmic streaming.

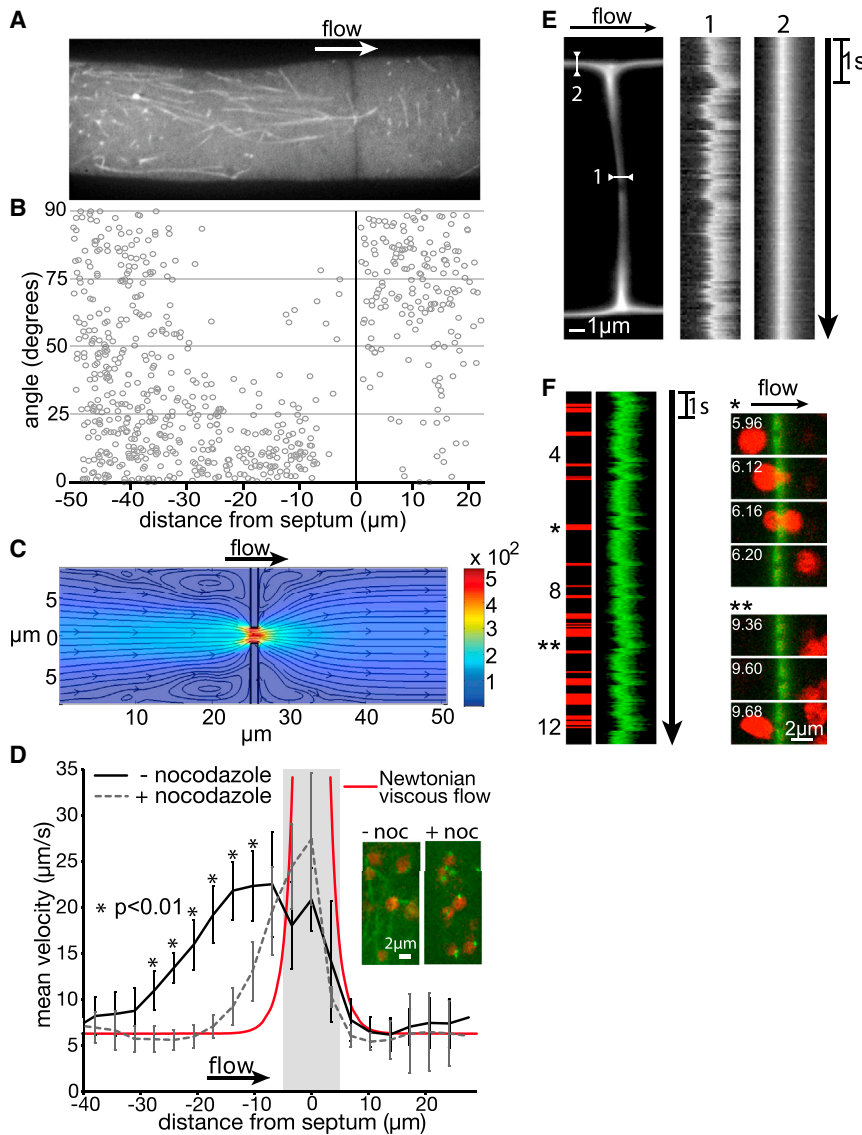


Figure 3. Behavior of Flowing Microtubules

(A) The image shows a single frame from a movie documenting the flow of microtubules. The arrow indicates the direction of flow. This figure is related to [Movie S3](#).

(B) The orientation of microtubules is determined for each frame of [Movie S3](#). A microtubule that is perpendicular to the long axis of the hypha has a value of 90 degrees.

(C) Computational 2D simulation shows time-averaged fluid flow in the presence of a cross-bundle of microtubules. For clarity, microtubules are not shown. Note the presence of upstream eddies and asymmetric flow. Fluid streamlines are included for visualization. Colormap indicates fluid velocity in $\mu\text{m/s}$. See [Experimental Procedures](#) for additional information.

(D) Flow asymmetry is significantly diminished by microtubule depolymerization. The graph shows the instantaneous mean velocity of nuclei (y axis) as a function of distance from the septum (x axis). The inset shows the appearance of cytoplasmic microtubules (green) and nuclei (red) under the indicated conditions. Scale bar represents $2\ \mu\text{m}$. The flow profiles are derived from eight movies each for nocodazole treated and untreated hyphae. Error bars indicate standard deviation. The asterisk identifies positions where there is a statistically significant difference between the two datasets (t test, $p < 0.01$). The red curve indicates the profile expected for Newtonian viscous flow. The gray box defines a region in close proximity to the pore where particle tracking tends to fail due to flow convergence and high velocity. The individual flow profiles can be found in [Figure S1](#).

(E) Flow-associated vibration of the septum. The kymographs document cell wall vibration near the septal pore (1) and at the lateral cell wall (2). Scale bar represents $1\ \mu\text{m}$. This figure is related to [Movie S4](#). (F) Septum deflection is caused by passing nuclei. Deflection of the septum (green) is associated with the presence of nuclei in the pore (red). This is the case for most (*) but not all of the observed deflections (**). Scale bar represents $2\ \mu\text{m}$. This figure is related to [Movie S5](#). Please see [Experimental Procedures](#) for additional information.

SPA-19 displays significant homology to the budding yeast Hos4 protein, which encodes a peripheral component of the Class I Set3C/Hos2 histone deacetylase complex (HDAC) (Pijnappel et al., 2001). In yeast and filamentous fungi, this HDAC is required for the induction of dynamically regulated genes (Baidyaroy et al., 2001; Wang et al., 2002; Hnisz et al., 2012). We examined the phenotype of the four *Neurospora* HDACs (Smith et al., 2010) and found that only deletion of the *Neurospora* *hos2* ortholog, *hda-2*, results in similar subapical pore degeneration (Figure 4A). The *hda-2* mutant also grows slowly (Figure 4A), suggesting that it participates in additional functions. To determine whether the enzymatic activity of HDA-2 is required for septal pore maintenance, we mutated catalytic residues required for HDAC activity (Wang et al., 2002), and found that this mutant phenocopies the deletion strain (Figures 4B–4D). Thus, septal pore maintenance requires the HDA-2 HDAC activity and is likely to be linked with regulated gene expression.

Eddy-Trapped Nuclei Are Differentiated from Flowing Nuclei

To further probe the relationship between HDA-2 and SPA-19, we pulled down HDA-2 and identified associated proteins by mass spectrometry (Figure 5A). Prominent associated proteins include SPA-19, SNT-1, and SIF-2. HDA-2 homologs in budding yeast (Pijnappel et al., 2001) and filamentous fungi (Ding et al., 2010) interact with the same proteins, indicating that this complex is highly conserved. We next tagged each of these proteins at their endogenous loci with eGFP and found that all four are localized to nuclei. Remarkably, nuclei found in eddies accumulate bright speckles of SPA-19 and associated factors as compared to nuclei found outside of the eddy (Figure 5B). This is observed in primary, but not secondary hyphae, suggesting that it depends on flow. These differentiated nuclei appear to occur in the region of cytoplasm that lies between the septum cell cortex and eddy-trapped vacuoles (Figure 5C and [Movie S6](#)). Thus, despite sharing a common cytoplasm, nuclei trapped

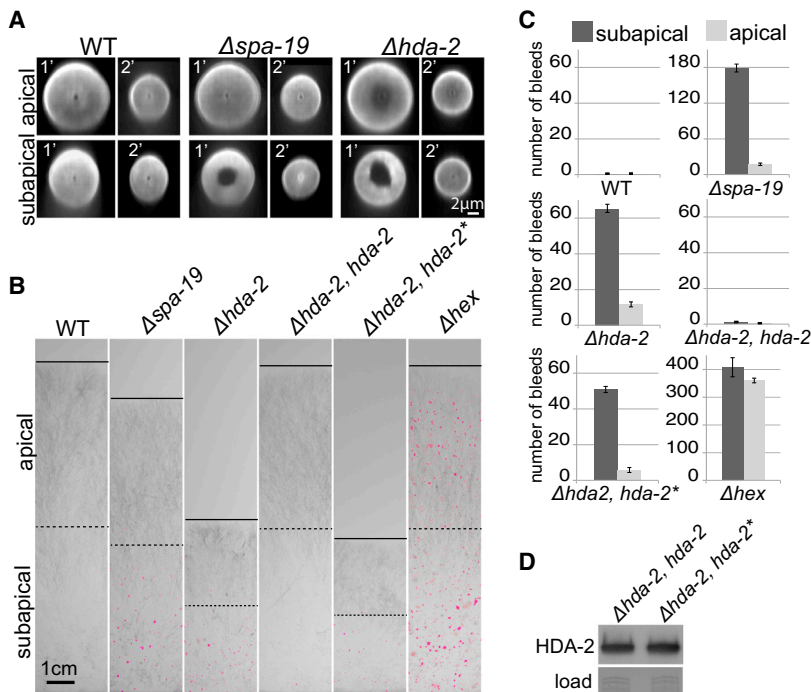


Figure 4. Flow-Associated Degeneration of the Septum in the *spa-19* Mutant

(A) Septa in the indicated strains are reconstructed from Z-stacks for primary (1') and secondary (2') hyphae. Scale bar represents 2 μ m.

(B) Protoplasmic bleeding. The indicated strains were grown on solid medium containing the dye Phloxine B, which stains protoplasmic scabs red. The *hda-2* catalytic dead mutant is denoted as *hda-2**. The growth front is indicated with a solid line and the midpoint used to define apical and subapical regions of the colony is shown with a dotted line. Scale bar represents 1 cm.

(C) Bleeding is quantified in apical and sub-apical regions of the colony as defined in (B). Note that the *hex* mutant has lost Woronin body function throughout the colony and thus produces scabs in both apical and subapical regions. Error bars indicate SD.

(D) Western blotting confirms that HDA-2 and HDA-2* are expressed at equal levels. Coomassie staining bands (load) confirm equal loading.

within eddies can become differentiated from streaming nuclei based on the accumulation of SPA-19 and associated proteins.

In some cases, eddy-trapped nuclei appear to be in close contact with one another. Time-lapse movies show that nuclei arrive at eddies from the flow and rapidly adhere to one another to produce multinucleate aggregates (Figures 5D and 5E and Movie S7). Initially, the contact area between a newly arriving nucleus and the nuclear aggregate is minimal. However, at a certain moment, the zone of adhesion rapidly spreads and the nucleus joins the aggregate (Figure 5E and Movie S7). These observations indicate that the eddy environment rapidly promotes an alteration in the behavior of nuclei.

Microtubule Activity Is Associated with Nuclear Differentiation

To investigate how microtubules influence nuclei, we simultaneously imaged both. These data show that flowing nuclei are embedded in an extensive array of microtubules that emanate from nuclear SPBs (Figures 6A and 6B; Movie S8). These microtubules can also make contacts with the cell cortex, and mediate the upstream movement of cortex-associated nuclei (Figures 2D and 6C). Nuclear aggregates also possess associated microtubules. However, in comparison with flowing microtubules, these are short and apparently restrained in their length by contact with the cell cortex and eddy-trapped vacuoles (Figure 6B).

Eddy-trapped vacuoles appear to insulate eddy-trapped nuclei from the flow. Evidence of this is observed in Movie S8 when an eddy-trapped vacuole is partly swept through the pore. Soon thereafter, the eddy-trapped nuclear aggregate engages flowing microtubules and is swept through the pore (Figure 6D). Nuclear aggregates can also move out of the eddy when hyphae arrest growth. Under this condition they begin to produce dynamic microtubule-associated protrusions (Figures 6E

tightly packed cortex-associated arrays on the upstream side of the septum (Figure 6G). This further indicates that microtubules favor retention of nuclei in flow and counteract their immobilization within the eddy region. Together, these data suggest that differential microtubule activity is a primary factor distinguishing the behavior of flowing and eddy-trapped nuclei.

Identification of SPA-19-Dependent Genes

Data presented thus far show that eddy-trapped nuclei accumulate HDA-2 and SPA-19, which are required for the maintenance of septa engaged in vigorous streaming. We next asked how these factors might contribute to the stability of the septum. In yeast as well as filamentous fungi, HDA-2 orthologs are required for the expression of dynamically regulated genes associated with taxa-specific developmental and physiological programs (Baidyary et al., 2001; Wang et al., 2002; Ding et al., 2010; Hnisz et al., 2012). To investigate a potential role in gene expression, we used RNA sequencing (RNA-seq) to compare *spa-19* mutant and wild-type expression profiles. Of genes downregulated in the *spa-19* mutant by a 4-fold change or greater, 8 of 20 have been shown to be cell wall associated in *Neurospora* or other fungal systems and 17 possess signal sequences and/or transmembrane domains (Table S1). These data suggest that SPA-19 acts at the level of gene expression, and possibly exerts its effect by promoting the expression of genes encoding proteins that act on the cell wall.

To verify misregulation at the level of protein, we selected a group of SPA-19 regulated genes encoding known cell wall proteins: *ncw-7* (Maddi et al., 2009), *pir-1* (Mrsa and Tanner, 1999; Mrsá et al., 1997), and *phi-a* (Schachtschabel et al., 2012). qPCR confirmed RNA-seq data (Figure 7A), and homologous recombination was used to produce epitope tagged proteins encoded by endogenous loci. In cellular extracts, each of these

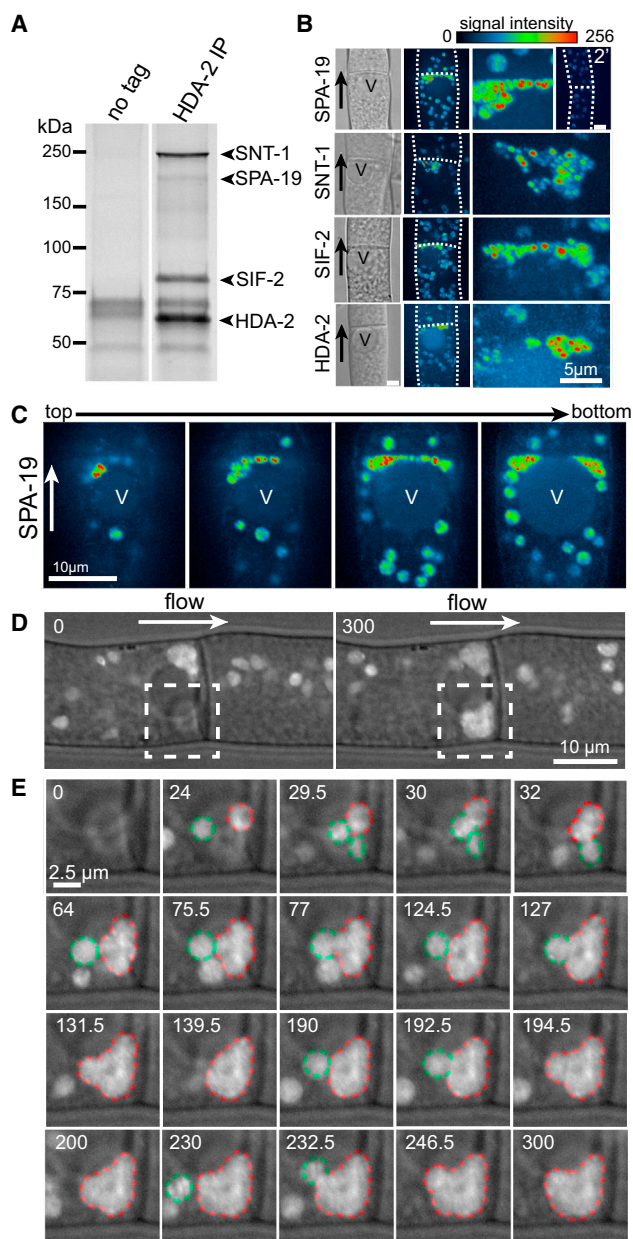


Figure 5. Differentiation of Nuclei in the Eddy Niche

(A) HDA-2 associated proteins are identified by immunoprecipitation of an HA-tagged version of HDA-2 and mass spectrometry.

(B) SPA-19 and associated proteins accumulate in speckles in eddy-trapped nuclei. The indicated genes were tagged at their endogenous loci and their localization was determined by confocal microscopy. Signal intensity is coded by the indicated color scale. Eddy-trapped vacuoles are labeled with V and the direction of flow is indicated by the arrows. Scale bar represents 5 μm .

(C) Spatial relationship between eddy-trapped nuclei containing SPA-19 speckles and the vacuole (V). Individual frames from a z stack show nuclei wedged between the septum and vacuole. Signal intensity is coded by the same scale shown in part B. Scale bar represents 10 μm . This figure is related to [Movie S6](#).

(D) Formation of an eddy-trapped nuclear aggregate. The upper panels show the beginning (0 s) and end (300 s) of the movie. The box indicates the region magnified in the lower panels. Scale bar represents 10 μm .

(E) Frames corresponding to the indicated time points are shown. Newly arriving nuclei are outlined with a dotted green line and the growing aggregate is outlined with a red dotted line. Time is indicated in seconds. This figure is related to [Movie S7](#).

proteins shifts to a lower molecular weight upon treatment with the deglycosylating enzyme Endoglycosidase H (Endo H), and this is consistent with their trafficking through the secretory pathway (Figure 7B). When cell extracts are produced from hyphae grown on solid medium where streaming is extensive, all three proteins are found at low levels in the *spa-19* mutant as compared with wild-type hyphae. In contrast, they are not misregulated when hyphae are grown in liquid medium where streaming is not observed (Figure 7C). Single and double deletion mutants of these particular genes do not display septum degeneration (data not shown), suggesting that they execute overlapping functions, or act in concert with other SPA-19 regulated genes. Together, these data define a role for SPA-19 in the regulation of gene expression and identify candidates for SPA-19 dependent effectors of septum reinforcement.

DISCUSSION

This paper identifies a cellular subcompartment that emerges because of regimented cytoplasmic streaming. In the *Neurospora* hypha, cytoplasm streams directionally from cell to cell to produce regions of relatively stagnant cytoplasm that occur where the septum meets the lateral cell wall (Figure 2). We find that nuclei immobilized within these eddies differentiate from flowing nuclei by aggregating (Figure 7), and accumulating SPA-19 and other HDA-2 associated components (Figure 6).

Flowing nuclei are embedded within a microtubule network and do not appear to come into close contact with one another. By contrast, nuclei arriving in the eddy can form tight adhesions to make multinucleate aggregates. These nuclei are not dynamic, but begin to produce microtubule-associated protrusions soon after exiting the eddy (Figures 6D and 6E). Inhibition of microtubules results in an aberrant accumulation of cortex-associated nuclei on the upstream side of the septum (Figure 6G), and this further shows that cytoplasmic microtubules counteract immobilization of nuclei on the upstream side of the septum. Together, these observations conform to the idea that regional variations in microtubule dynamics emerge because of flow, and determine differences in nuclear behavior. Eddy-trapped vacuoles can shield trapped nuclei from capture by streaming microtubules (Figure 6C and [Movie S8](#)), and thereby further reinforce the eddy niche.

Flow approaches the septum in a long converging path and exits in a wider diverging path. This pattern does not conform to that of a Newtonian fluid and is in part determined by the tendency of microtubules to become extended and entrain flow approaching the pore (Figures 3A and 3B). This is supported by computer simulation (Figure 3C), and microtubule depolymerization, which significantly diminishes flow asymmetry (Figure 3D). Interestingly, when dilute polymer solutions are subjected to flow through an orifice, they produce an asymmetric flow pattern with vortices similar to those observed in the hypha. (Lipscomb et al., 1988; Mongruel and Cloitre, 2003; Szabo et al., 1997). This shows that hydrodynamic properties of flowing polymers can indeed be sufficient to promote flow asymmetry (Figure 3F). However, in the hypha, microtubule depolymerization does not entirely abolish flow asymmetry (Figure 3D). Thus, additional aspects of this system contribute to the patterning of flow. Likely candidates include other cytoplasmic

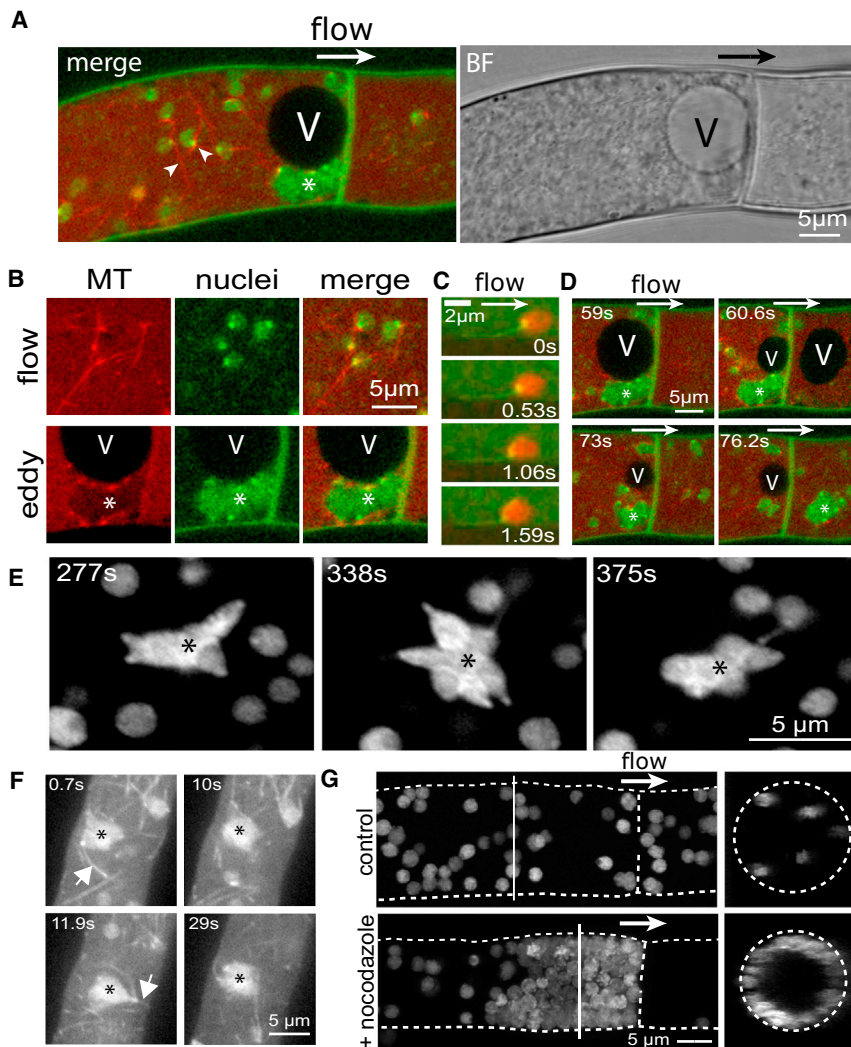


Figure 6. Relationship between Nuclei and Microtubules

(A) Flowing nuclei are embedded within a microtubule network (arrowheads). The merge of microtubule (red) and nuclear (green) signals is shown on the left and the bright field view (BF) is shown on the right. The eddy-trapped nuclear aggregate is marked with an asterisk and the vacuole is labeled with V. Scale bar represents 5 μm. The direction of flow is indicated with the arrow. This figure is related to [Movie S8](#).

(B) Microtubules associated with eddy-trapped nuclei are short. Isolated views of flowing (flow) and eddy-trapped nuclei (eddy) are shown. Microtubule (MT) and nuclear (nuclei) signals are separated for clarity. The nuclear aggregate is marked with an asterisk and the vacuole is labeled with a V. Scale bar represents 5 μm.

(C) A cortex-associated nucleus moves against the flow. The microtubules are green and the nucleus is red. Time is indicated in seconds. Scale bar represents 2 μm.

(D) An eddy trapped nuclear aggregate (asterisk) enters the flow. Frames extracted from [Movie S8](#) show an eddy trapped vacuole and nuclear aggregate being swept through the pore. The direction of flow is indicated with the arrow. Time is indicated in seconds. The vacuole is marked with a V. Scale bar represents 5 μm.

(E) Nuclear aggregates that dissociate from the eddy produce dynamic extensions. Three frames labeled in seconds are shown. Scale bar represents 2.5 μm. This figure is related to [Movie S9](#).

(F) Nuclear aggregates that dissociate from the eddy make dynamic contacts with microtubules. Microtubules are indicated with white arrows and the nuclear aggregate is marked with an asterisk. Time is indicated in seconds. Scale bar represents 5 μm.

(G) Microtubule depolymerization causes nuclei to accumulate aberrantly on the upstream side of the septum. The micrographs show hyphae grown in

the absence (upper) or presence of nocodazole (lower). Left: maximum projection of nuclei. The dotted line indicates the outline of the hypha and septum. The solid white line defines the position of the orthogonal view shown on the right. The direction of flow is indicated with the arrow. Scale bar represents 5 μm.

polymers, complex interactions between organelles and the restriction on organelle flow imposed by the pore ([Figure 3F](#)).

Eddies form due to the constraint on flow imposed by the septal pore. Flow-dependent subcompartments can be envisioned in other cell types where regimented streaming occurs. For example, in the plant phloem, long distance pressure-driven flow occurs through perforate sieve plates that interconnect sieve elements ([Mullendore et al., 2010; Savage et al., 2013](#)). In other plant cells, a self-organizing actomyosin network produces complex patterns of circulatory streaming ([Woodhouse and Goldstein, 2013](#)). In this case, flowing microtubules are unlikely to pattern subcompartments. Nevertheless, as in the hypha, positional information embodied in flow patterns could be exploited to instruct cellular activities. We speculate that cytoplasmic constituents are likely to vary in the degree to which they associate with motors and their associated organelles. This variation combined with differing tendencies to come to rest in regions where flow is restricted may be sufficient to produce biochemically distinct subcompartments.

Vigorous cytoplasmic streaming imparts significant mechanical force to the septum ([Figures 3D and 3E](#)), which breaks down in the absence of SPA-19 and HDA-2 ([Figure 4](#)). In other fungi, the orthologous HDAC is required for the induction of genes associated with diverse developmental programs ([Baidyaroy et al., 2001; Ding et al., 2010; Hnisz et al., 2012; Wang et al., 2002](#)). The *spa-19* mutant fails to induce a group of genes specifically under conditions that promote streaming. These are enriched for secreted cell wall proteins and because the septum is known to be a site of secretion ([Hayakawa et al., 2011](#)), this provides one plausible mechanism for active reinforcement of the septum. However, the mechanism of septum reinforcement is likely to be complex and more work will be required to understand precisely how SPA-19 and HDA-2 protect the septum from degeneration. In *Aspergillus niger*, neighboring hyphae can present distinct gene expression profiles ([de Bekker et al., 2011](#)). As with data presented here, this conforms with the idea that the genetic identity of hyphal segments is not solely determined by age and environment. We anticipate that continued investigation of

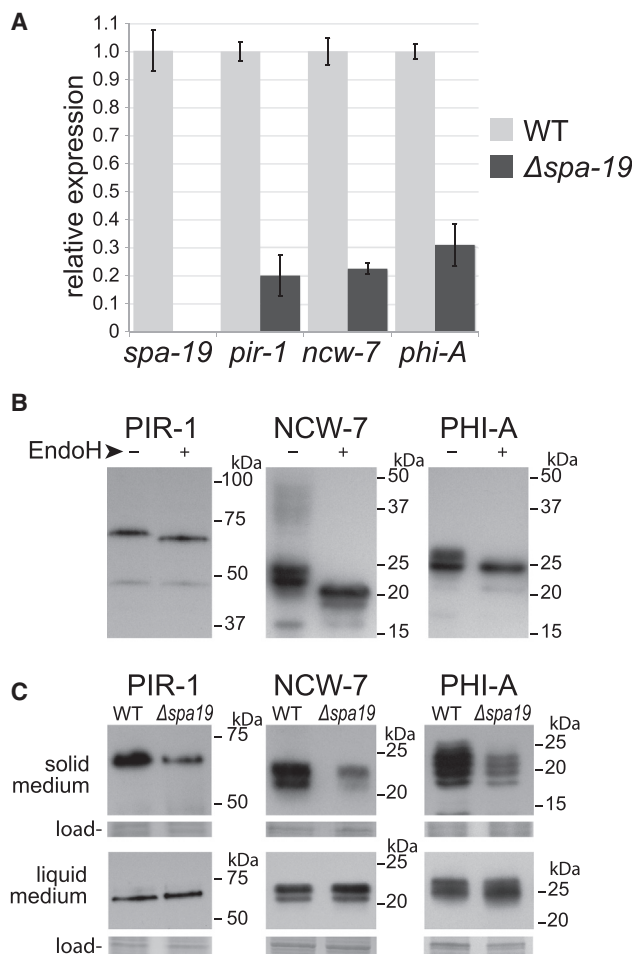


Figure 7. A Group of Secreted Cell Wall Proteins Require *spa-19* for Appropriate Expression

(A) qPCR indicates that the indicated genes encoding secreted cell wall proteins are not appropriately expressed in the *spa-19* mutant background. This figure is related to Table S1. Error bars indicate SD.

(B) Secreted cell wall proteins are glycosylated. Extracts were prepared from strains expressing the indicated HA-epitope tagged proteins expressed from their endogenous loci. Extracts were treated with (+) or without (-) Endo H and analyzed by SDS-PAGE and western blotting.

(C) Tagged cell wall proteins in the indicated strains were grown on either solid (upper) or liquid (lower) medium and whole cell extracts were analyzed by SDS-PAGE and anti-HA western blotting. Coomassie blue stained bands provide a loading control (load).

hyphal cytoplasmic streaming will reveal general mechanisms that link physiological processes with the genetic reinforcement of cellular identity.

EXPERIMENTAL PROCEDURES

Neurospora Strains and Methods

Neurospora strains were grown and maintained on synthetic Vogel's N medium (VN) and genetic crosses were carried out on synthetic crossing medium (SC) as previously described (Davis and de Serres, 1970). Unless otherwise indicated, *Neurospora* deletion strains (Colot et al., 2006) were obtained from the Fungal Genetics Stock Center (<http://www.fgsc.net>). For depolymerization of microtubules, nocodazole (Sigma-Aldrich) was maintained at 10 mg/ml in DMSO and added to the growth medium at a final concentration

of 2.2 μ M. Microtubules and nuclei were labeled by expressing β -tubulin-GFP and histone H1-GFP fusion proteins, respectively (Freitag et al., 2004). Peroxisomes were tagged with mCherry-PTS1 as previously described (Liu et al., 2011). *spa-19* (NCU00388), *hda-2* (NCU02795), *snt-1* (NCU10346), and *sif-2* (NCU06838) were tagged with GFP at endogenous loci by marker fusion tagging (MFT) (Lai et al., 2010). For 3X HA tagging of *pir-1* (NCU07569), *ncw-7* (NCU08907), and *phi-A* (NCU00399), the tag was introduced to the chromosomal locus using DNA fragments produced by fusion PCR and homologous recombination. These fragments were designed to create in-frame C-terminal fusions. For selection, the dominant marker hygromycin phosphotransferase gene (*hph*) under control of the pTRPc promoter was introduced downstream of the gene of interest, except in the case of the *phi-A* where *panB* from *Aspergillus nidulans* was used (Ng et al., 2009). To epitope tag *hda-2*, a genomic fragment encompassing *hda-2* was modified to encode a C-terminal 3X HA tag and cloned into the plasmid pOKE104. The histone deacetylase dead version of HDA-2 (H240A, H241A) was also produced in this plasmid. These two constructs were transformed into a $\Delta hda-2$, *pan-2* mutant background and strains expressing similar levels of protein were identified by anti-HA western blotting. Strains, plasmids, and oligonucleotides can be found in the Supplemental Experimental Procedures.

For quantification of cytoplasmic blebbing, the indicated *Neurospora* strains were grown in the dark on VN medium with 7.5 mg/ml phloxine B at 30°C for 2 days, photographed, and analyzed as described below. Growth rate measurements were carried out in race tubes fashioned from plastic 25 ml pipettes filled with VN medium. Growth was initiated from one end of the race tube using equal amounts of conidia and measurements were made once the maximum growth rate was established. The average with standard deviation is shown for three independent experiments.

RNA Sequencing

Neurospora strains were grown on solid VN medium in 90 mm diameter Petri dishes in the dark at room temperature (25°C). The following day, approximately 5 mm \times 20 mm blocks of mycelium were cut with a scalpel from approximately 5 mm behind the growth front and transferred to one end of approximately 20-mm wide strips of solid VN medium running down the middle of 90 mm diameter Petri dishes. To minimize the induction of asexual spores, which is stimulated by light, this manipulation was done in the dark and under a photographic red safelight. These strips were grown in the dark at room temperature overnight. The next day a 15-mm wide block of agar encompassing the growth front was excised with a scalpel and submerged immediately into liquid nitrogen. The agar blocks were ground in liquid nitrogen using a mortar and pestle to produce a fine powder that was stored at -80°C. RNA was extracted from approximately 150 μ l of packed powder using the RNeasy Plant Mini kit (QIAGEN).

RNA-seq was carried using Illumina HiSeq 2000 at the Huntsman Cancer Institute, University of Utah. RNA-seq FASTQ sequence files were processed with sickle (<https://github.com/najoshi/sickle>) to filter and trim reads for low quality (trimming bases with Phred score <20) and requiring minimum length of 30 base pair reads. Only read pairs where both pairs met the quality and length threshold were carried forward. Overall quality of the sequencing reads were evaluated with FastQC (<http://www.bioinformatics.babraham.ac.uk/projects/fastqc/>) and found to be within acceptable scores. The trimmed RNA-seq reads were aligned to the genome with tophat (2.0.2) using the parameter b2-sensitive and using bowtie2. The *Neurospora crassa* v10 genome assembly (Nc10) and annotation (<http://broadinstitute.org>) was used. Expression values per gene were computed with cufflinks using Nc10 annotation and comparisons for significant differences in expression evaluated with cuffdiff (Trapnell et al., 2012).

qRT-PCR

RNA was extracted from the same material used for RNA-seq using the Arcturus PicoPure RNA Isolation Kit (Applied Biosystems) according to manufacturer instructions. Purified RNA was treated with DNase using the Ambion DNA-freeTM Kit (Life Technologies). The GoScriptTM Reverse Transcription System (Promega) was used to prepare cDNA. qRT-PCR was carried out on an ABI 7900HT Fast Real-Time PCR System, using the GoTaq qPCR Master Mix (Promega) and the results were normalized to actin.

HDA-2-3X HA Pull-Down

To prepare the hyphal extract, a frozen powder of ground mycelium was prepared as previously described (Chen et al., 2014). Ten milliliters of IP buffer (20 mM HEPES [pH 7.5], 350 mM NaCl, 10% glycerol, 0.1% Tween20 [vol/vol], 1 mM PMSF, complete mini EDTA-free protease inhibitor [Roche]) was added to an equal volume of frozen mycelial powder, which was then thawed on ice for 10 min with periodic vortexing. The mixture was centrifuged at $500 \times g$ through a 40 μm cell strainer (BD Biosciences) for 5 min. The supernatant was then centrifuged at $16,000 \times g$ for 30 min. This supernatant was then incubated at 4°C for 1 hr with anti-HA antibody (Roche) coupled Dynabeads (Invitrogen). The beads were subsequently washed according to the manufacturer's instructions and eluted with HPH-EB (0.5 mM NH_4OH , 0.5 mM EDTA) and dried overnight in a SpeedVac (Eppendorf). The pull-down was analyzed by SDS-PAGE and mass spectrometry was used to identify the indicated bands.

EndoH Treatment

HA-tagged *Neurospora* strains were grown on either liquid or solid VN medium and mycelial powder was prepared as described above. The powder was re-suspended in a 5-volume equivalent of $2 \times$ SDS-PAGE loading buffer, boiled for 5 min, and centrifuged for 1 min at $16,000 \times g$. Ten microliters of supernatant was digested with EndoH (New England BioLabs) at 37°C for 1 hr. The samples were boiled for 10 min, followed by centrifugation for 1 min at $16,000 \times g$. Equivalent amounts of EndoH treated and untreated samples was then subjected to SDS-PAGE and anti-HA western blotting using a horseradish peroxidase (HRP)-conjugated rat monoclonal anti-HA antibody (Roche) at 1:2,500 dilution.

Microscopy and Image Analysis

For movies of streaming through primary hyphae, conidia were inoculated at the periphery of 90 mm Petri dishes containing solid VN medium. These were grown overnight in the dark at 25°C to 30°C and imaging was initiated when the colony had grown a little over halfway across the plate. An approximately 15 mm \times 30 mm block of agar was excised from the colony to include several mm of medium in front of the apical hyphae (hyphae are parallel to the long axis of this block). This block was transferred to a microscope slide and gently overlaid with a coverslip. This procedure results in a transient grow arrest. After 20 to 30 min hyphae approximately 5 to 10 mm behind the growth front were selected for imaging based on their degree of streaming. In Figure 4A, the cell wall was labeled with calcofluor white (Sigma-Aldrich) at a concentration of 1 $\mu\text{g}/\text{ml}$. In Figures 6A, 6B, 6D, and 6F, nuclei were labeled with Hoechst 33258 (Sigma-Aldrich) at a concentration of 10 $\mu\text{g}/\text{ml}$.

High-speed imaging (Figures 3A, 3E, 5D, 5E, 6C, and 6F) was done using a Microlambda spinning disk (Nikon Ti-E microscope, Hamamatsu Orca-Flash 4 camera) controlled by Metamorph software (Molecular Devices). A Leica SP8 microscope was used for z stacks and when two color imaging was required. The movie shown in Figure 1 was obtained using a Nikon SMZ1500 stereomicroscope equipped with a Coolsnap HQ camera (Photometrics) controlled by Metamorph software. Image editing and quantification was done using ImageJ (NIH). Growth measurement in Figures 1A and 1B was done using the mTrackJ plugin in ImageJ. For peroxisome and nuclei tracking in Figure 2, movies were analyzed using the particle-tracking module of Imaris software (BitPlane). Scatterplot showing position and velocity were built in Excel (Microsoft). Kymographs in Figure 3 were produced using MultipleKymograph plugin in ImageJ. Quantification of protoplasmic bleeding shown in Figure 4C was done after applying a threshold based on phloxine B staining using the particle analysis function in ImageJ. Microtubule angle measurements in Figure 6B were done manually in imageJ.

To quantify nuclear velocity in Figure 3D, raw movies were rotated in ImageJ to make flow parallel to the x axis. Noise was reduced using the "Remove Outliners" ImageJ filter. Instantaneous nuclear velocity and position was measured using the Imaris software tracking module (autoregressive motion algorithm) and exported to Excel using the Imaris Vantage module. Nuclei with a velocity below 3 $\mu\text{m}/\text{s}$ were considered non-flowing and excluded from analysis. To calculate average velocity profiles, eight hyphae for each nodazole treated and untreated hyphae displaying similar flow rates were analyzed. Average velocity profiles were obtained by dividing each hypha into 20 equal sections along the x axis (3.45 μm slices) and averaging all veloc-

ity measurements for each section. Individual profiles were then combined to obtain a single velocity profile per condition. The measurement of skewness associated with these profiles is described in the following section.

Modeling Cytoplasmic Streaming

Consider the flow of a Newtonian fluid through a hyphal branch modeled as an axisymmetric cylinder, partitioned by a flat cross wall with a septal pore at its center. Because the Reynolds number is vanishingly small (Lew, 2005), the flow is viscous and Stokes equations apply. For a wall with finite thickness, the Hagen-Poiseuille contribution should be included, so that

$$Q_s = \left(3 + \frac{8h_s}{\pi R_s} \right)^{-1} \frac{R_s^3 \Delta p}{\mu}, \quad (\text{S1})$$

where Q_s is the pore volumetric flow rate, R_s is the pore radius, h_s is the septal thickness, Δp is the applied pressure difference, and μ is the cytoplasmic viscosity. The centerline flow velocity within the pore is simply

$$U_s = \frac{2Q_s}{\pi R_s^2}, \quad (\text{S2})$$

Neglecting osmotic fluid exchange with the external environment, the pore flow rate Q_s and the hyphal flow rate Q_h are equal. Accordingly, the pore size could be deduced through the flow velocity measurements via the following relationship:

$$\left(\frac{R_s}{R_h} \right)^2 = \frac{U_h}{U_s}, \quad (\text{S3})$$

where R_h and U_h are the radius and centerline flow velocity of the hypha branch respectively. We show the flow behavior of a Newtonian fluid through a model hypha using a numerical simulation. Figure 2C shows the flow profile through a model hyphal radius $R_h = 8 \mu\text{m}$, septal pore radius $R_s = 0.2 \mu\text{m}$ and septal wall thickness $h_s = 0.4 \mu\text{m}$, with a pressure gradient imposed so that the centerline velocity at the inlet is $U_{s,inlet} \approx 20 \mu\text{m}/\text{s}$. For clarity, the maximum velocity magnitude shown in the colormap is limited to 350 $\mu\text{m}/\text{s}$.

To quantify the asymmetry of nuclear flow (Figure 3D), we used skewness. This is a statistical measure for characterizing the degree of asymmetry of a distribution. Because the recorded data are evenly distributed over a defined interval, we used the following formula to obtain this value,

$$\text{Skewness} = \frac{N}{(N-1)(N-2)} \sum \left(\frac{X - \bar{X}}{S} \right)^3, \quad (\text{S4})$$

where N is the number of data points, X is the value of a data point, \bar{X} is the mean and S is the standard deviation.

Modeling Cytoplasmic Streaming in the Presence of Microtubules

To investigate the possibility that the observed asymmetry in cytoplasmic flow is patterned by streaming microtubules, we simulated a Newtonian fluid flowing through a 2D model septum, the flow interacting with a cross-bundle of microtubules (length = 7.5 μm). For modeling, we used the immersed boundary method (Peskin, 2002), which is frequently employed in simulating hydrodynamic interactions of flexible filaments (Huang et al., 2007), such as cilia (Dillon et al., 2007) and DNA (Zhang et al., 2012). Here, the bending stiffness of the microtubule used in the model is $\sim 5 \times 10^{24} \text{ N/m}^2$ (Yang et al., 2008) and compares well with physical ranges $\sim 1\text{--}10 \times 10^{24} \text{ N/m}^2$ (Ghavanloo et al., 2010). Figure 3C shows the time-averaged pattern of flow produced by such a computational 2D simulation.

Calculation of Pressure Difference Associated with Septum Vibration

Due to its relatively small size, the septal pore is intermittently plugged by nuclei and other larger streaming cytoplasmic content, causing a transient buildup of pressure across the septum (Figures 3D and 3E). The pressure difference is balanced by the bending stress created by a spontaneous deflection of the septum described by the Kirchhoff-Love plate theory. Using clamped boundary conditions, the displacement of the septum is estimated as,

$$w \sim \frac{R_s^4 \Delta p}{64D}, \quad (\text{S5})$$

where Δp is the increased pressure difference and R_d is the deformable radius of the septum. The material constant is given by $D = 2h_s^3 E / 3(1 - \nu^2)$, where h_s is the septal wall thickness, E is the Young modulus and ν is the Poisson ratio. Based on the following physical estimates: $h_s \sim 0.4 \mu\text{m}$, $R_d \sim 6 \mu\text{m}$, $w \sim 0.75 \mu\text{m}$ (by experimental inspection Figure 3D), $E \sim 110 \text{ Mpa}$ (based on mean experimental measurements by (Zhao et al., 2005) and $\nu \sim 0.5$ (for an incompressible material), we estimate the pressure difference across the septum as approximately 2.3 bar. This value compares well and is within the hydrostatic pressure of the hypha of approximately 4–5 bar (Lew et al., 2004).

SUPPLEMENTAL INFORMATION

Supplemental Information includes Supplemental Experimental Procedures, one figure, one table, and nine movies and can be found with this article online at <http://dx.doi.org/10.1016/j.devcel.2015.07.017>.

AUTHOR CONTRIBUTIONS

L.P., J.L., R.A.L., and G.J. conceived and performed experiments. F.Y.L. and K.-H.C. conducted mathematical analysis and computer simulations. J.S. analyzed RNA-seq data. G.J. wrote the manuscript with input from all coauthors.

ACKNOWLEDGMENTS

We thank Tu Anh Nguyễn for critical reading of the manuscript. We gratefully acknowledge the use of deletion mutants generated by NIH grant P01 GM068087 “Functional Analysis of a Model Filamentous Fungus.” F.Y.L. and K.-H.C. are supported by the Agency for Science, Technology and Research (A*STAR), Singapore. Research in the Jedd Group is supported by the Temasek Life Sciences Laboratory.

Received: March 5, 2015

Revised: May 26, 2015

Accepted: July 30, 2015

Published: August 24, 2015

REFERENCES

- Abadeh, A., and Lew, R.R. (2013). Mass flow and velocity profiles in *Neurospora* hyphae: partial plug flow dominates intra-hyphal transport. *Microbiology* 159, 2386–2394.
- Baidyaroy, D., Brosch, G., Ahn, J.H., Graessle, S., Wegener, S., Tonukari, N.J., Caballero, O., Loidl, P., and Walton, J.D. (2001). A gene related to yeast HOS2 histone deacetylase affects extracellular depolymerase expression and virulence in a plant pathogenic fungus. *Plant Cell* 13, 1609–1624.
- Bleichrodt, R., Vinck, A., Krijgsheld, P., van Leeuwen, M.R., Dijksterhuis, J., and Wösten, H.A.B. (2013). Cytosolic streaming in vegetative mycelium and aerial structures of *Aspergillus niger*. *Stud. Mycol.* 74, 31–46.
- Brangwynne, C.P., Eckmann, C.R., Courson, D.S., Rybarska, A., Hoeghe, C., Gharakhani, J., Jülicher, F., and Hyman, A.A. (2009). Germline P granules are liquid droplets that localize by controlled dissolution/condensation. *Science* 324, 1729–1732.
- Buller, A.H.R. (1933). The translocation of protoplasm through the septate mycelium of certain Pyrenomycetes, Discomycetes and Hymenomyces. In *Researches on Fungi*, volume V, A.H.R. Buller, ed. (Longmans), pp. 75–167.
- Chen, Y., Pieuchot, L., Loh, R.A., Yang, J., Kari, T.M.A., Wong, J.Y., and Jedd, G. (2014). Hydrophobic handoff for direct delivery of peroxisome tail-anchored proteins. *Nat. Commun.* 5, 5790.
- Colot, H.V., Park, G., Turner, G.E., Ringelberg, C., Crew, C.M., Litvinkova, L., Weiss, R.L., Borkovich, K.A., and Dunlap, J.C. (2006). A high-throughput gene knockout procedure for *Neurospora* reveals functions for multiple transcription factors. *Proc. Natl. Acad. Sci. USA* 103, 10352–10357.
- Davis, R.H., and de Serres, F.J. (1970). Genetic and microbiological research techniques for *Neurospora crassa*. *Methods Enzymol.* 27, 79–143.
- de Bekker, C., Bruning, O., Jonker, M.J., Breit, T.M., and Wösten, H.A.B. (2011). Single cell transcriptomics of neighboring hyphae of *Aspergillus niger*. *Genome Biol.* 12, R71.
- Dillon, R.H., Fauci, L.J., Omoto, C., and Yang, X. (2007). Fluid dynamic models of flagellar and ciliary beating. *Ann. N Y Acad. Sci.* 1107, 494–505.
- Ding, S.-L., Liu, W., Iliuk, A., Ribot, C., Vallet, J., Tao, A., Wang, Y., Lebrun, M.-H., and Xu, J.-R. (2010). The tig1 histone deacetylase complex regulates infectious growth in the rice blast fungus *Magnaporthe oryzae*. *Plant Cell* 22, 2495–2508.
- Freitag, M., Hickey, P.C., Raju, N.B., Selker, E.U., and Read, N.D. (2004). GFP as a tool to analyze the organization, dynamics and function of nuclei and microtubules in *Neurospora crassa*. *Fungal Genet. Biol.* 41, 897–910.
- Ghavanloo, E., Daneshmand, F., and Amabili, M. (2010). Prediction of bending stiffness and deformed shape of non-axially compressed microtubule by a semi-analytical approach. *J. Biol. Phys.* 36, 427–435.
- Goehring, N.W., Trong, P.K., Bois, J.S., Chowdhury, D., Nicola, E.M., Hyman, A.A., and Grill, S.W. (2011). Polarization of PAR proteins by advective triggering of a pattern-forming system. *Science* 334, 1137–1141.
- Goldstein, R.E., Tuval, I., and van de Meent, J.-W. (2008). Microfluidics of cytoplasmic streaming and its implications for intracellular transport. *Proc. Natl. Acad. Sci. USA* 105, 3663–3667.
- Hayakawa, Y., Ishikawa, E., Shoji, J.-Y., Nakano, H., and Kitamoto, K. (2011). Septum-directed secretion in the filamentous fungus *Aspergillus oryzae*. *Mol. Microbiol.* 81, 40–55.
- Hecht, I., Rappel, W.-J., and Levine, H. (2009). Determining the scale of the Bicoid morphogen gradient. *Proc. Natl. Acad. Sci. USA* 106, 1710–1715.
- Hepler, P.K., Vidali, L., and Cheung, A.Y. (2001). Polarized cell growth in higher plants. *Annu. Rev. Cell Dev. Biol.* 17, 159–187.
- Hnisz, D., Bardet, A.F., Nobile, C.J., Petryshyn, A., Glaser, W., Schöck, U., Stark, A., and Kuchler, K. (2012). A histone deacetylase adjusts transcription kinetics at coding sequences during *Candida albicans* morphogenesis. *PLoS Genet.* 8, e1003118.
- Huang, W.X., Shin, S.J., and Sung, H.J. (2007). Simulation of flexible filaments in a uniform flow by the immersed boundary method. *J. Comput. Phys.* 226, 2206–2228.
- Hyman, A.A., and Brangwynne, C.P. (2011). Beyond stereospecificity: liquids and mesoscale organization of cytoplasm. *Dev. Cell* 21, 14–16.
- Jedd, G., and Chua, N.H. (2000). A new self-assembled peroxisomal vesicle required for efficient resealing of the plasma membrane. *Nat. Cell Biol.* 2, 226–231.
- Kato, M., Han, T.W., Xie, S., Shi, K., Du, X., Wu, L.C., Mirzaei, H., Goldsmith, E.J., Longgood, J., Pei, J., et al. (2012). Cell-free formation of RNA granules: low complexity sequence domains form dynamic fibers within hydrogels. *Cell* 149, 753–767.
- Lai, J., Ng, S.K., Liu, F.F., Patkar, R.N., Lu, Y., Chan, J.R., Suresh, A., Naqvi, N., and Jedd, G. (2010). Marker fusion tagging, a new method for production of chromosomally encoded fusion proteins. *Eukaryot. Cell* 9, 827–830.
- Lai, J., Koh, C.H., Tjota, M., Pieuchot, L., Raman, V., Chandrababu, K.B., Yang, D., Wong, L., and Jedd, G. (2012). Intrinsically disordered proteins aggregate at fungal cell-to-cell channels and regulate intercellular connectivity. *Proc. Natl. Acad. Sci. USA* 109, 15781–15786.
- Lee, C., Zhang, H., Baker, A.E., Occhipinti, P., Borsuk, M.E., and Gladfelter, A.S. (2013). Protein aggregation behavior regulates cyclin transcript localization and cell-cycle control. *Dev. Cell* 25, 572–584.
- Lew, R.R. (2005). Mass flow and pressure-driven hyphal extension in *Neurospora crassa*. *Microbiology* 151, 2685–2692.
- Lew, R.R. (2011). How does a hypha grow? The biophysics of pressurized growth in fungi. *Nat. Rev. Microbiol.* 9, 509–518.
- Lew, R.R., Levina, N.N., Walker, S.K., and Garrill, A. (2004). Turgor regulation in hyphal organisms. *Fungal Genet. Biol.* 41, 1007–1015.
- Lipscomb, G.G., Denn, M.M., Hur, D.U., and Boger, D.V. (1988). The flow of fiber suspensions in complex geometries. *J. Non-Newton. Fluid Mech.* 26, 297–325.

- Liu, F., Lu, Y., Pieuchot, L., Dhavale, T., and Jedd, G. (2011). Import oligomers induce positive feedback to promote peroxisome differentiation and control organelle abundance. *Dev. Cell* *21*, 457–468.
- Maddi, A., Bowman, S.M., and Free, S.J. (2009). Trifluoromethanesulfonic acid-based proteomic analysis of cell wall and secreted proteins of the ascomycetous fungi *Neurospora crassa* and *Candida albicans*. *Fungal Genet. Biol.* *46*, 768–781.
- Mongruel, A., and Cloitre, M. (2003). Axisymmetric orifice flow for measuring the elongational viscosity of semi-rigid polymer solutions. *J. Non-Newt. Fluid Mech.* *110*, 27–43.
- Mrsa, V., and Tanner, W. (1999). Role of NaOH-extractable cell wall proteins Ccw5p, Ccw6p, Ccw7p and Ccw8p (members of the Pir protein family) in stability of the *Saccharomyces cerevisiae* cell wall. *Yeast* *15* (10A), 813–820.
- Mrsá, V., Seidl, T., Gentzsch, M., and Tanner, W. (1997). Specific labelling of cell wall proteins by biotinylation. Identification of four covalently linked O-mannosylated proteins of *Saccharomyces cerevisiae*. *Yeast* *13*, 1145–1154.
- Mullendore, D.L., Windt, C.W., Van As, H., and Knoblauch, M. (2010). Sieve tube geometry in relation to phloem flow. *Plant Cell* *22*, 579–593.
- Ng, S.K., Liu, F., Lai, J., Low, W., and Jedd, G. (2009). A tether for Woronin body inheritance is associated with evolutionary variation in organelle positioning. *PLoS Genet.* *5*, e1000521.
- Palacios, I.M., and St Johnston, D. (2002). Kinesin light chain-independent function of the Kinesin heavy chain in cytoplasmic streaming and posterior localisation in the *Drosophila* oocyte. *Development* *129*, 5473–5485.
- Peskin, C.S. (2002). The immersed boundary method. *Acta Numer.* *11*, 1–39.
- Pijnappel, W.W., Schaft, D., Roguev, A., Shevchenko, A., Tekotte, H., Wilm, M., Rigaut, G., Séraphin, B., Aasland, R., and Stewart, A.F. (2001). The *S. cerevisiae* SET3 complex includes two histone deacetylases, Hos2 and Hst1, and is a meiotic-specific repressor of the sporulation gene program. *Genes Dev.* *15*, 2991–3004.
- Ramos-García, S.L., Roberson, R.W., Freitag, M., Bartnicki-García, S., and Mouriño-Pérez, R.R. (2009). Cytoplasmic bulk flow propels nuclei in mature hyphae of *Neurospora crassa*. *Eukaryot. Cell* *8*, 1880–1890.
- Roper, M., Simonin, A., Hickey, P.C., Leeder, A., and Glass, N.L. (2013). Nuclear dynamics in a fungal chimera. *Proc. Natl. Acad. Sci. USA* *110*, 12875–12880.
- Savage, J.A., Zwieniecki, M.A., and Holbrook, N.M. (2013). Phloem transport velocity varies over time and among vascular bundles during early cucumber seedling development. *Plant Physiol.* *163*, 1409–1418.
- Schachtschabel, D., Arentshorst, M., Lagendijk, E.L., and Ram, A.F. (2012). Vacuolar H(+)-ATPase plays a key role in cell wall biosynthesis of *Aspergillus niger*. *Fungal Genet. Biol.* *49*, 284–293.
- Smith, K.M., Dobosy, J.R., Reifsnnyder, J.E., Rountree, M.R., Anderson, D.C., Green, G.R., and Selker, E.U. (2010). H2B- and H3-specific histone deacetylases are required for DNA methylation in *Neurospora crassa*. *Genetics* *186*, 1207–1216.
- Szabo, P., Rallison, J.M., and Hinch, E.J. (1997). Start-up of flow of a FENE-fluid through a 4: 1: 4 constriction in a tube. *J. Non-Newt. Fluid Mech.* *72*, 73–86.
- Tominaga, M., Kimura, A., Yokota, E., Haraguchi, T., Shimmen, T., Yamamoto, K., Nakano, A., and Ito, K. (2013). Cytoplasmic streaming velocity as a plant size determinant. *Dev. Cell* *27*, 345–352.
- Trapnell, C., Roberts, A., Goff, L., Pertea, G., Kim, D., Kelley, D.R., Pimentel, H., Salzberg, S.L., Rinn, J.L., and Pachter, L. (2012). Differential gene and transcript expression analysis of RNA-seq experiments with TopHat and Cufflinks. *Nat. Protoc.* *7*, 562–578.
- Trinci, A.P.J. (1973). Influence of the width of the peripheral growth zone on the radial growth rate of fungal colonies on solid media. *J. Gen. Microbiol.* *67*, 325–344.
- Wang, A., Kurdistani, S.K., and Grunstein, M. (2002). Requirement of Hos2 histone deacetylase for gene activity in yeast. *Science* *298*, 1412–1414.
- Woodhouse, F.G., and Goldstein, R.E. (2013). Cytoplasmic streaming in plant cells emerges naturally by microfilament self-organization. *Proc. Natl. Acad. Sci. USA* *110*, 14132–14137.
- Yang, X., Dillon, R.H., and Fauci, L.J. (2008). An integrative computational model of multiciliary beating. *Bull. Math. Biol.* *70*, 1192–1215.
- Yi, K., Unruh, J.R., Deng, M., Slaughter, B.D., Rubinstein, B., and Li, R. (2011). Dynamic maintenance of asymmetric meiotic spindle position through Arp2/3-complex-driven cytoplasmic streaming in mouse oocytes. *Nat. Cell Biol.* *13*, 1252–1258.
- Zhang, Y., de Pablo, J.J., and Graham, M.D. (2012). An immersed boundary method for Brownian dynamics simulation of polymers in complex geometries: application to DNA flowing through a nanoslit with embedded nanopits. *J. Chem. Phys.* *136*, 014901.
- Zhao, L., Schaefer, D., Xu, H., Modi, S.J., LaCourse, W.R., and Marten, M.R. (2005). Elastic properties of the cell wall of *Aspergillus nidulans* studied with atomic force microscopy. *Biotechnol. Prog.* *21*, 292–299.